

# Design of structured $\text{La}_{2-x}\text{Sr}_x\text{CuO}_{4+y}$ films as superconducting transition-edge sensors at 4.2K

M.M. Botana<sup>1</sup>, A.S. Viz<sup>2</sup>, M.V. Ramallo<sup>1,\*</sup>

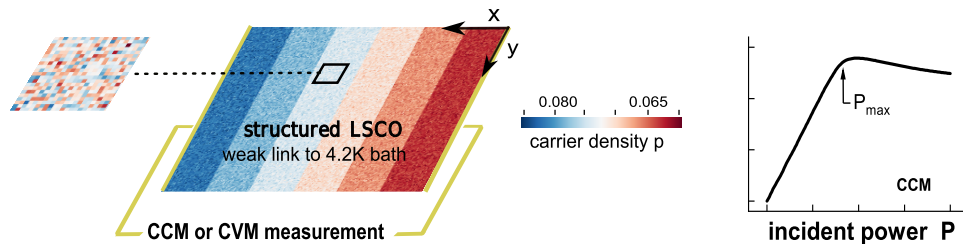
<sup>1</sup>QMatterPhotonics, Department of Particle Physics and Institute of Materials iMATUS, University of Santiago de Compostela 15782, Spain.

<sup>2</sup>QMatterPhotonics, Department of Particle Physics, University of Santiago de Compostela 15782, Spain.

\*Corresponding author (mv.ramallo@usc.es)

**Abstract:** We calculate the effects of carrier-density structuration and patterning on thin films of the cuprate superconductor  $\text{La}_{2-x}\text{Sr}_x\text{CuO}_{4+y}$ , in order to optimize its functional characteristics as sensing material for resistive transition-edge bolometers at liquid-He temperature. We perform finite-element computations considering two major contributions to structuration: The intrinsic random nanoscale disorder associated to carrier density nonstoichiometry, plus the imposition of regular arrangements of zones with different nominal carrier densities. Using ad-hoc seek algorithms, we obtain various structuration designs that markedly improve the bolometric performance, mainly the saturation power and dynamic range. Bolometric operation becomes favorable even in the easier-to-implement constant current mode of measurement.

*Graphical Abstract:*



*Keywords:*

Bolometers, radiation detectors, transition-edge sensors, structured cuprate superconductor thin films.

# 1 Introduction

Sensing devices based on novel superconducting surfaces [1–5] such as transition-edge sensors (TES) are employed in multiple fields of research and technology for detection of radiation, for instance in contexts where broad bandwidth and high sensitivity is primordial and refrigerated operation is feasible or even desirable [6–9]. Some examples of application are astrophysics (cosmic background radiation, etc.) [10, 11], avionics and satellite technology (for environmental imaging, etc.) [12, 13], neutron detection for fusion research [14], etc. Also the current emergence of quantum technologies of information, often requiring cryogenics to limit quantum decoherence effects, is increasing the interest in TES to discriminate photonic signals. [15–17]

Most existing TES use conventional low-temperature superconductors with very sharp transitions, commonly in thin film or microwire form and operated in constant-voltage mode (CVM) to limit their thermal runaway. [18] However, using a cuprate superconductor as sensing material may potentially bring new options of design. [19–23] The probably best-known options for using cuprates in TES devices involve operating them slightly below its mean-field critical temperature  $T_c$ , often with liquid-N<sub>2</sub> cryogenics and sometimes using a non-ohmic regime of their electrical resistivity and sensitive amplifiers to achieve readout of the response to incoming radiation. [19–23]

In a recent paper, [24] we made a first exploration of a novel route to further optimize the use of cuprate thin films in TES applications. We considered custom designs of micro- and nano-scale planar spatial variations of the local carrier concentration  $p(\vec{r})$ , seeking to modify the profile of the  $R(T)$  transition (the electrical resistance versus temperature near the superconducting transition) and thus the corresponding bolometric operational parameters: mainly the temperature coefficient of resistance  $\text{TCR}=R^{-1}dR/dT$  and the saturation power  $P_{\text{max}}$  (or rather equivalently its ratio with the minimum detectable power, *i.e.*, the linear dynamic range  $\text{DR}=P_{\text{max}}/P_{\text{min}}$ ). The cuprates simulated in [24] were YBa<sub>2</sub>Cu<sub>3</sub>O<sub>7- $\delta$</sub>  (YBCO) thin films with different planar variations  $p(\vec{r})$  (that are experimentally achievable, *e.g.*, through spatial variations of the oxygen index  $\delta(\vec{r})$  for which various techniques do exist [25–27]). The best obtained  $p(\vec{r})$  designs move the operating temperature to the value 77 K (convenient for liquid-N<sub>2</sub> cryogenics), allow operation in a region with simple ohmic response readable

with conventional electronics and provide, *e.g.*, about double TCR and one order of magnitude larger DR than non-structured films. [24,28]

However, for some applications 77 K is not the most desirable operating temperature. Liquid-He temperature 4.2 K may be preferred, so to reduce the thermal noise or because the advantageous values of heat capacity and thermal conductivities of the whole TES setup (that affect aspects such as the recovery time, often depending on temperature-dependent characteristics of the supporting substrates and thermal links rather than on the sensing superconductor itself). [6–14] Therefore, it is interesting to seek for possible  $p(\vec{r})$  structuration designs that optimize cuprates for their use in TES sensors designed for operating temperature 4.2 K.

With that aim, in the present paper we explore designs for micro- and nano-structurations of  $p(\vec{r})$  in thin films of the cuprate  $\text{La}_{2-x}\text{Sr}_x\text{CuO}_{4+y}$  (LSCO). In this material, various methods have been experimentally demonstrated to change the carrier concentration  $p$ , with 4.2 K well within the range of attainable critical temperatures. [29–34] This includes not only variation of the  $x$  and/or  $y$  stoichiometry indexes during sample growth, [34] but also using techniques able of variable local actuation, and hence  $p(\vec{r})$  patterning, such as, *e.g.*, focused ion-beam direct writing, [35,36] local long-time SEM exposition, [37,38] or surface modification via tip-based scanning microscopies like STM [25] or heated-tip AFM [39].

When considering LSCO, various differences and similarities with respect to the case of YBCO have to be considered from the beginning. Firstly, the variation of the  $R(T)$  curves with the carrier concentration  $p$  are qualitatively different, with LSCO developing for the so-called underdoped  $p$ -values ( $p < 0.16$ ) a smaller and negative TCR at temperatures above the fluctuation transition rounding, [29] while for overdoped  $p > 0.16$  it remains positive [29,30,40] (in contrast, in YBCO [29,32,40] the TCR is always positive but the  $p > 0.16$  range is not fully accessible by change of the chemical index  $\delta$ ). Also the fluctuation rounding of the  $R(T)$  transition is qualitatively different, as the more pronounced anisotropy and 2D-character of LSCO increase the critical exponents and, notably, the importance of the lower tail of the  $R(T)$  transition, due to the Kosterlitz-Thouless phenomenon. [41,42] In addition, the dependence of the critical temperature itself with doping,  $T_c(p)$ , has in both compounds a similar general

dome-like behavior centered around  $p = 0.16$  but in the vicinity of  $p = 0.125$  there is in LSCO a pronounced local depression, versus a smooth plateau in YBCO. [43–45] (Also heat capacities near  $T_c$  are different [46], mainly due to the temperatures at which they must be evaluated). On the other hand, both materials share the significant importance of disorder effects that, as shown, *e.g.*, in [24, 34, 47] and will be also confirmed in this paper, will be key in the TES behavior of the structured material.

The outline of this paper is as follows: In Sect. 2 we describe the methods implemented by us; this includes Subsect. 2.1 on the modeling of  $R(T)$  for a given carrier concentration  $p$ , Subsect. 2.2 on the modelization of local variations  $p(\vec{r})$  (composed of both imposed designs  $\bar{p}(\vec{r})$  plus Gaussian random disorder effects  $p_{\text{disord}}(\vec{r})$ ), and Subsect. 2.3 on our computational methods for seeking optimal  $p(\vec{r})$  and calculating their corresponding bolometric parameters (TCR, DR, etc.). In Sect. 3 we describe our results when considering the non-patterned case, both for underdoped and overdoped  $\bar{p}$ -values (and also compare them against some existing  $R(T)$  measurements that in this first simple case are available). In Sect. 4 we describe our results for spatial patterns optimizing the bolometric performance for the underdoped case, finding in particular that some spatial pattern designs lead to much better bolometric performance than the non-patterned surfaces (including, *e.g.*, one order of magnitude larger saturation power and correspondingly larger DR; see Table 1). In Sect. 5 we present our corresponding results for overdoped carrier densities, where again we propose some spatial patterns of much improved bolometric performance (even somewhat better than those of the underdoped case; see also Table 1). These results suggest that structured LSCO thin films with ad-hoc planar structurations are promising as sensing surfaces for TES bolometers at liquid-He temperature. Finally, in our concluding Sect. 6 we comment on some aspects that we believe could ease the application of our calculations to eventual efforts to experimentally produce such ad-hoc TES sensing surfaces.

## 2 Methods to find optimal carrier density structures of LSCO thin films for better bolometric sensing performance at 4.2K

### 2.1 Resistive transition of the base non-structured film

In order to obtain the electrical resistance transition  $R(T)$  of a LSCO film with a given spatial map of carrier concentrations  $p(\vec{r})$ , we shall use in this work finite-element computations with each simulation cell having a single local value of  $p$ . Thus, a needed starting point is the resistance to be associated to each of those elements. Fortunately, extensive measurements and theory comparisons do exist in the literature in LSCO samples of well-controlled and highly homogeneous values of  $p$ , that will serve us as valid phenomenological equations for our purposes. The critical temperature, the normal-state behavior, and the resistivity rounding near the transition are the three aspects to be considered for such resistance curves for each  $p$ . We describe those aspects below.

#### 2.1.1 Critical temperature $T_c$ as a function of carrier density $p$

It is well-known that the  $T_c(p)$  dependence in LSCO and other cuprates is dome-like, with maximum value reached at  $p = 0.16$  (the so-called optimal doped  $p$ -value). [40] Also that this dome is somewhat altered around  $p = 1/8$ , where a further depression of  $T_c$  happens (likely due to stripe order matching [48, 49]). As shown in [44], for LSCO films this can be accurately accounted for by the empirical formula:

$$T_c(p) = T_c^{\text{opt}} \left[ \left( 1 - \frac{p-0.16}{0.11} \right)^2 \right] - \delta T_{c1/8} \exp \left[ - \left( \frac{p-1/8}{0.01} \right)^2 \right]. \quad (1)$$

Regarding the values of  $T_c^{\text{opt}}$  and  $\delta T_{c1/8}$  let us note already here that in this paper we shall use material parameters corresponding to LSCO films of thickness 100 nm grown over (100)SrTiO<sub>3</sub> substrates, a typical morphology appropriate for TES applications. This corresponds to  $T_c^{\text{opt}} = 23\text{K}$  and  $\delta T_{c1/8} = 4.8\text{K}$ . [44, 50] (We also note already here that we shall defer to Sect. 6 on a discussion on the parameter values and other considerations that should be fine-tuned in our numerical analyses to extend them to LSCO films not matching exactly our default parameter choices, like film thickness,

etc. Moderate quantitative, but not qualitative, differences are obtained in our final results when considering changes in such assumed details.)

### 2.1.2 Normal-state contribution to the electrical resistivity

It is customary [41–43, 51–56] to describe the electrical resistivity  $\rho$  of superconductors at temperatures above and near  $T_c$  as two separate additive contributions to its reciprocal, the electrical conductivity, in particular as  $\rho^{-1} = \rho_n^{-1} + \Delta\sigma$  where  $\rho_n$  is the normal-state resistivity, that may be obtained from measurements well above  $T_c$ , and  $\Delta\sigma$  is the so-called paraconductivity, or fluctuation conductivity, producing a rounding near  $T_c$  of the  $\rho(T)$  transition.

Regarding  $\rho_n$ , in cuprate superconductors its phenomenology as a function of  $T$  and  $p$  is today quite comprehensibly described at the empirical experimental level [29, 30, 32, 43] (even if the reason for such phenomenology is famously not yet truly understood, being a problem almost as open as the origin of the high  $T_c$  itself [43, 57]). Following standard practice, [29, 30, 42, 43] will use the following formulas:

$$lll\rho_n(T, p \leq 0.15) = A(p) + B(p)T + C(p)T^2 + D(p)/T, \quad (2)$$

$$\rho_n(T, p > 0.15) = A(p) + B(p)T + C(p)T^2. \quad (3)$$

For the coefficients  $A(p)$ ,  $B(p)$ ,  $C(p)$  and  $D(p)$  we will use the numerical values that result from fitting the extensive set of experimental measurements in LSCO films reported for  $p \leq 0.22$  by Ando *et al.* [29] and for  $p > 0.23$  by Cooper *et al.* [30], and interpolate them for the intermediate  $p$  values. We performed these fits in the region  $30 \text{ K} \lesssim T \lesssim 150 \text{ K}$  (because for lower temperatures the resistivity data may be affected by the rounding due to critical fluctuations near the transition, as we discuss in the next subsection).

### 2.1.3 Paraconductivity contribution

Regarding the  $\Delta\sigma$  contribution to  $\rho^{-1}$ , for cuprates again ample literature exist (see, *e.g.*, [42, 47, 54, 55]) proposing equations that phenomenologically describe it with excellent accuracy (irrespective of possible differences in the theory interpretations, or

even the existence of alternative formulas possibly also able to accurately describe these data [51]). We will employ in this paper the same set of equations as we used in [42] for previous studies of  $\Delta\sigma$  in LSCO films as a function of doping, covering the whole range of temperatures where the rounding of the transition is observed, including: the lower tail of the transition, associable [40–42] with a Kosterlitz-Thouless (KT) regime of the fluctuations; the main transition region around the  $\rho(T)$  inflection point, associable [51, 54, 55] with the Gaussian regime of the fluctuations; and the high-temperature part of the rounding, extending up to about  $2T_c$  and describable [56] in terms of short-wavelength, or high-energy, fluctuations. As shown in [42], the following equations are in excellent agreement with observations in those regions:

$$lcl\Delta\sigma = A_{\text{KT}} \exp \sqrt{4 \frac{T_c - T_{\text{KT}}}{T - T_{\text{KT}}}} \quad \text{for } T_{\text{KT}} < T < T_{\text{Gi}}, \quad (4)$$

$$\Delta\sigma = \frac{e^2}{16\hbar d \varepsilon} \left(1 - \frac{\varepsilon}{\varepsilon^c}\right)^2 \quad \text{for } T_{\text{Gi}} \leq T \leq T^c. \quad (5)$$

The parameters involved in these equations, and numerical values for them in agreement [42] with data in LSCO films, are as follows:  $T_c$  is the mean-field critical temperature (given by Eq. 1 in LSCO films);  $T_{\text{KT}}$  is the Kosterlitz-Thouless temperature (located in the tail of the transition, found in LSCO films to be well approximated by  $T_c - 2\text{K}$  [42]);  $T_{\text{Gi}}$  is the Ginzburg temperature (the boundary above  $T_c$  between the KT and Gaussian fluctuation regimes,  $T_{\text{Gi}} = 1.015 T_c$  in LSCO films [42, 58]);  $T^c$  is the cutoff temperature well above the transition where fluctuation effects become negligible, that we may take as  $T^c = 1.7T_c$ ;<sup>1</sup> [42, 51–53]  $\varepsilon = \ln(T/T_c)$  is a reduced temperature;  $\varepsilon^c = \ln(T^c/T_c)$ ;  $d$  is the distance between superconducting layers (6.6 Å in LSCO [34, 44]) and  $A_{\text{KT}}$  is a proportionality constant that may be obtained by equating Eqs. 4 and 5 at  $T = T_{\text{Gi}}$ . [42, 47]

## 2.2 Consideration of spatial maps of local carrier density: nominal pattern and disorder contributions

The main subject of study of the present work is LSCO films with a spatial variation  $p(\vec{r})$  of carrier concentrations, instead of the homogeneous  $p$  value assumed above. We

---

<sup>1</sup>Actually, in [42] it is found a larger value for  $T^c$  in the underdoped case, but  $T^c = 1.7T_c$  fits well the data also in that case when restricting the analyses to  $T < 30\text{K}$ , as in our present paper.

shall consider in what follows two sources of  $p(\vec{r})$  variation, namely:

$$p(\vec{r}) = \bar{p}(\vec{r}) + p_{\text{disord}}(\vec{r}), \quad (6)$$

where  $\bar{p}(\vec{r})$  is the nominal carrier concentration map, *i.e.*, the ad-hoc pattern externally imposed by the experimentalist using any structuration procedure of choice (*e.g.*, focused ion-beam direct writing, local SEM oxidation, etc.) and  $p_{\text{disord}}(\vec{r})$  is a spatially random contribution related to the unavoidable disorder in any actual LSCO sample (a pictorial view of this two-scale structuration is given in our graphical abstract).

The main objective of the present paper is to research the  $\bar{p}(\vec{r})$  patterns optimizing the bolometric performance. Note, however, that considering the  $p_{\text{disord}}(\vec{r})$  contribution is also crucial for an accurate description of the resistivity in the transition region. This has been shown to be the case even for the best homogeneous LSCO films grown by different experimentalists (see, *e.g.*, Fig. 7 of [44]). The reason for the unavoidable appearance of the  $p_{\text{disord}}(\vec{r})$  contributions even for non-patterned (*i.e.*,  $\bar{p}(\vec{r})=\text{const}$ ) films may be traced to the non-stoichiometry of the carrier concentrations (in the superconducting range  $0.05 \lesssim p \lesssim 0.27$ , where as always we express  $p$ -values normalized as number of carriers per  $\text{CuO}_2$  unit cell) that in turn implies that the spatial distribution of carrier donors is nonuniform at the few-unit-cells scale. The statistics of such minimum (or intrinsic) disorder may be calculated using coarse-grained averages (see [34, 44]), resulting for LSCO in a Gaussian distribution with full-width at half-maximum

$$\Delta p_{\text{disord}} = 0.0162 \sqrt{\bar{p} - \bar{p}^2/2}. \quad (7)$$

The number prefactor results from considering a coarse-grain average size of  $(30 \text{ nm})^2$ , in agreement with direct measurements [59] of the spatial charge distribution in cuprates.<sup>2</sup>

### 2.3 Numerical computation of $R(T)$ of the structured superconducting films and algorithmic search of structurations optimized for bolometric performance

Let us describe our computational methods to calculate for each structured film its  $R(T)$  curve, and also our algorithms to search the  $\bar{p}(\vec{r})$  patterns that best optimize the

---

<sup>2</sup>It is easy to translate the  $p$  distribution into a  $T_c$  one, of which magnetic susceptibility measurements allow direct experimental probe. As shown in [34, 44], such measurements in LSCO samples by different authors do present  $T_c$  distributions in accordance with Eq. 7.



bolometric performance when the film is used as a TES sensor element.

To calculate  $R(T)$  we perform a finite-element modeling of the film, in which we assign to each spatial node  $i$  of the simulation a single  $p_i$  value and a corresponding  $R_i(T)$ . For the  $p(\vec{r}_i)$  map we shall consider both the nominal and disorder contributions, as in Eq. 6. We then used in-house software to calculate, using a  $200 \times 200$  finite-element mesh-current matrix method, the global resistivity of the entire nonhomogeneous film. This involves, for each temperature and pattern, inverting matrices of about  $10^4$  non-null elements. This task can be parallelized for which we employ a custom cluster (16 GPU cards with more than 2500 floating-point calculators each, allocated to this calculation exclusively, so the computing effort may be maintained over several weeks). An automated script automatically generates different nominal charge concentration patterns, adds the disorder contributions, launches their  $R(T)$  simulations, and selects the nominal pattern maps that yield the best performance for bolometric sensing.

In the case of LSCO, as mentioned above, each  $T_c$  monodomain is estimated to be of area  $(30 \text{ nm})^2$ . [34, 44, 59]. Then our  $200 \times 200$  finite-element mesh corresponds to  $(6 \mu\text{m})^2$ , an area similar to the microsensor TES devices implemented by several authors. [20, 21, 60–62]. We checked in a random selection of our simulations that increasing the underlying mesh to  $400 \times 400$  elements strongly increments the computation time but leads to the same results.

We tried different algorithms to generate the different nominal charge concentration patterns  $\bar{p}(\vec{r})$ . We obtained our best results from one of the simplest options, consisting in considering samples composed of a finite number  $N$  of successive slices, transversal to the current's direction, each with carrier concentration  $\bar{p}_j$  following a general power law in the slice number  $j$ , and commanding the algorithm to scan values for the parameters  $\bar{p}_{\min}$ ,  $\bar{p}_{\max}$ ,  $N$ ,  $\beta$  and  $\gamma$  for the power law when written as:

$$\bar{p}_j = \bar{p}_{\min} + \left[ \frac{\bar{p}_{\max} - \bar{p}_{\min}}{(N-1)^\beta} \right] j^\beta, \quad j = 0, \dots, N-1, \quad (8)$$

where each successive slice is of thickness  $x_{j+1} - x_j$  and

$$x_j = \Gamma \cdot (\bar{p}_j - \bar{p}_{\min})^\gamma, \quad j = 0, \dots, N. \quad (9)$$

(The normalization  $\Gamma$  is given by the film's length). In a second pass of optimization, the algorithm adds to Eqs. 8 and 9 small fine-tuning corrections of a few percent, to further

Table 1: Best obtained structurations for improved TES sensor performance.

structuration	$N$	$\bar{p}$		$\beta$	$\gamma$	TCR (K <sup>-1</sup> )	$P_{\min}$ (pW)		$P_{\max}$ ( $\mu$ W)		DR	
		$\bar{p}_{\min}$	$\bar{p}_{\max}$				CCM	CVM	CCM	CVM	CCM	CVM
UD-1 zone	1	0.060		-	-	2.2	0.47	9.5	10	5.0	2 $\cdot$ 10 <sup>4</sup>	5 $\cdot$ 10 <sup>2</sup>
UD-6 zone	6	0.060	0.082	1.0	1.23	3.5	0.29	28	83	55	3 $\cdot$ 10 <sup>5</sup>	2 $\cdot$ 10 <sup>3</sup>
UD-10 zone	10	0.060	0.109	1.0	1.23	3.0	0.33	38	140	100	4 $\cdot$ 10 <sup>5</sup>	3 $\cdot$ 10 <sup>3</sup>
OD-1 zone	1	0.260		-	-	2.7	0.38	11	15	10	4 $\cdot$ 10 <sup>4</sup>	9 $\cdot$ 10 <sup>2</sup>
OD-6 zone	6	0.231	0.255	0.80	1.55	3.5	0.20	8.0	87	50	4 $\cdot$ 10 <sup>5</sup>	6 $\cdot$ 10 <sup>3</sup>
OD-10 zone	10	0.160	0.255	0.57	3.40	3.5	0.28	11	190	60	7 $\cdot$ 10 <sup>5</sup>	6 $\cdot$ 10 <sup>3</sup>

The first group of columns indicates the parameters describing (via Eqs. 8 and 9) the best structurations found by our algorithms and simulations for the underdoped (UD) and overdoped (OD) case and for different number of pattern zones  $N$ . The second group summarizes the obtained bolometric parameters (see also Figs. 1 and 2) for both the constant current (CCM) and constant voltage (CVM) modes of operation. Note the increase in dynamic range DR achieved by progressive structuration, associated mainly to a increase of  $P_{\max}$  (without significant penalty in TCR and  $P_{\min}$ , that sometimes even improve modestly).

improve the best results identified in the first pass. The scanning formulas 8 and 9 are inspired by the results of our previous work for the superconductor YBCO, [24] as they have the parameter freedom to reproduce almost exactly the patterns found in that work to optimize the bolometric performance of that material (plus additional rather different shapes). Note that in the above formula the dependence of  $\bar{p}(\vec{r})$  is only in the axial coordinate  $x$ ; however, the additional disorder contribution  $p_{\text{disord}}(\vec{r})$  is 2D (again this is the same as in [24]; note also that this 2D character increases the order of magnitude of the computational effort but, as mentioned before, is crucial to obtain accurate results in cuprates).

To obtain the bolometric performance for each simulated film from its computed  $R(T)$  we calculate its response to an incoming radiation power. For that, we will use a common thermal model for TES devices (see, *e.g.*, [22, 63, 64]) to calculate their stationary state temperature  $T_s$  under such radiation:

$$P + P_{\text{self}}(T_s) = G \cdot (T_s - T_{\text{bath}}), \quad (10)$$

where  $P$  is the incoming radiation power,  $P_{\text{self}}$  is the self-generated power by Joule effect,  $T_{\text{bath}}$  is the bath temperature and  $G$  the thermal conductance of the link to that bath. In accordance with our focus in this paper we take  $T_{\text{bath}} = 4.2$  K, and a value  $G = 10^{-5}$  W/K typical [23] for bolometers at that temperature. (We are also making in Eq. 10 the common approximation of an optical absorptivity  $\eta = 1$ ; otherwise  $P$  in our

results should be interpreted as  $\eta P$  [64]). For  $P_{\text{self}}$ , we will perform our calculations in each of two possible operational modes of the sensor: constant-current mode (CCM) and constant-voltage mode (CVM). In them, [22]

$$ccrP_{\text{self}}(T) = I_{\text{bias}}^2 R(T) \quad \text{for CCM,} \quad (11)$$

$$P_{\text{self}}(T) = V_{\text{bias}}^2 / R(T) \quad \text{for CVM,} \quad (12)$$

where  $I_{\text{bias}}$  and  $V_{\text{bias}}$  are the bias current and voltage imposed in each mode. The CVM operation is often favored for TES devices that employ low-temperature superconductors, to moderate their problematic thermal runaways. [18] In high- $T_c$  cuprates these are not so much of an issue. [16, 17, 19, 22] The CCM is normally easier to implement than CVM (that often requires implementing very-low noise reading equipments such as SQUID devices [65]). For completeness, we shall study our proposed material optimizations in both CVM and CCM.

Combination of Eqs. 10 to 12 with the  $R(T)$  curve allows to calculate the output signal (intensity in CVM and voltage in CCM) produced by the sensor as a function of the incident optical power  $P$  (see Figs. 1 and 2).

From those results we obtain the quantities that, as noted in our Introduction, are the main parameters usually employed to discuss TES designs:  $P_{\text{min}}$ ,  $P_{\text{max}}$ , DR and TCR (see Table 1).

In particular, the temperature coefficient of resistance TCR for an incoming power  $P$  is given by  $\text{TCR} = R^{-1} \frac{\delta R}{\delta T}$  with  $\delta R = R(P) - R_{P=0}$  and  $\delta T = T(P) - T_{P=0}$ . As customary, [23, 64, 66] we will pursue a constant TCR value for all the operating range of incident power, what corresponds in practice to a linear dependence of  $R$  with  $T$  in that range. Therefore, we compute such single TCR value from the increments in the whole linear region:

$$\text{TCR} = \frac{1}{R(T_{\text{bath}})} \frac{R(T^+) - R(T_{\text{bath}})}{T^+ - T_{\text{bath}}}, \quad (13)$$

where  $T^+$  is the highest temperature up to which  $R(T)$  remains linear in  $T$  (see second column of Figs. 1 and 2).

The minimum and maximum incident radiation powers that the TES is able to sense,  $P_{\text{min}}$  and  $P_{\text{max}}$ , are obtained as follows: First we calculate, using Eqs. 1 to 12,

the measurable output (intensity in CVM and voltage in CCM) of the sensor to each  $P$  value (third and fourth columns of Figs. 1 and 2). Then we identify  $P_{\max}$  as the maximum power up to which that measurable output remains linear in  $P$  (in our results we will find that incoming powers beyond  $P_{\max}$  not only break the linearity of the sensor but also shortly saturate the measured output anyway; therefore, we did not consider the complication of extending the operation range through nonlinear behaviors).

To estimate the minimum detectable power,  $P_{\min}$ , in rigor the resolution and sensitivity of the equipment used to probe the electrical resistivity of the superconductor must be taken into account, and not only the response of the sensing material. Of course, much can be said about the state-of-art techniques to optimize that reading measurement [8, 23, 64–66] and in principle nothing prevents deploying them over the structured films studied here. However, for simplicity and ease of comparison we decided to fix, in our calculations, a modest relative measurement resolution of  $10^{-4}$  for both current and voltage signals, as easily attainable with conventional equipment. [65, 66] Using this common fixed reference will allow us to compare the performances of the different material structurations proposed in this paper with each other. For an example of experimental TES implementation with a similar resolution see, *e.g.*, [66].

Finally, the dynamic range is obtained as  $DR = P_{\max}/P_{\min}$ .

### 3 Results for non-patterned superconductors (*UD-1 zone, OD-1 zone*)

Let us first present our results for the bolometric performance of LSCO thin films without any imposed patterning (*i.e.*,  $\bar{p}(\vec{r})=\text{const}$ ), that are obviously the easiest to fabricate from the experimentalists' point of view. As in the rest of this paper, we seek operational temperatures of 4.2 K. This corresponds to either  $\bar{p} = 0.06$  (underdoped case) or  $\bar{p} = 0.26$  (overdoped). We label these cases in our figures and tables as *UD-1 zone* and *OD-1 zone* respectively (signaling the under/overdoped case and the number of planar regions with different  $\bar{p}$ ).

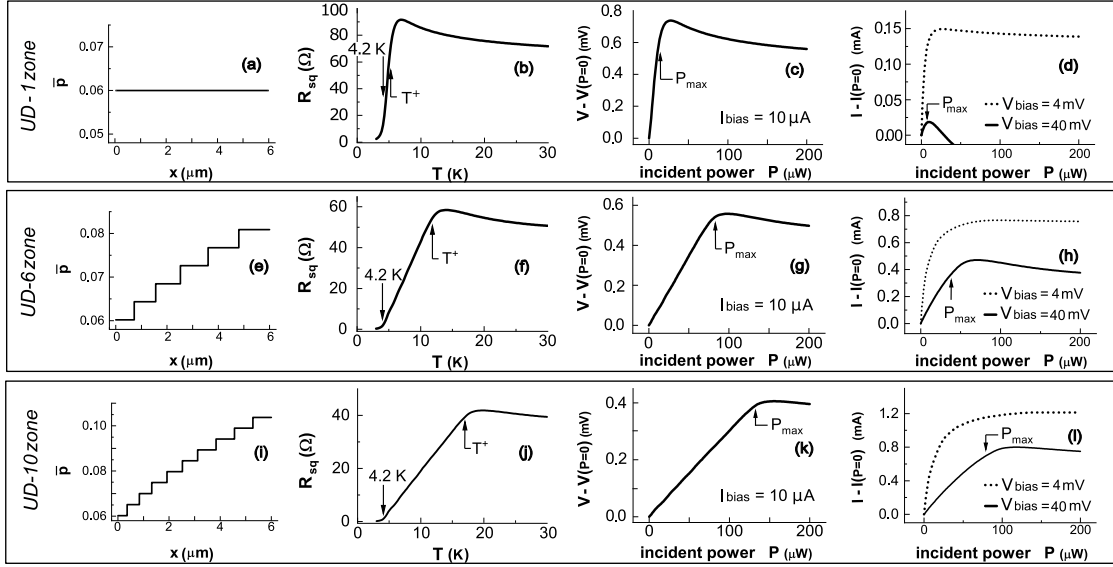


Figure 1: Results for sensing films with nominal carrier densities in the underdoped (UD) range  $\bar{p} < 0.16$ . First row corresponds to a non-patterned film ( $N = 1$ ). Subsequent rows correspond to films patterned with  $N = 6$  and  $10$  zones of  $\bar{p}$  (following Eqs. 8 and 9 with parameter values of Table 1). First column of graphs display  $\bar{p}$  vs. the longitudinal position, second column the electrical sheet resistance vs. temperature, third column the output voltage for fixed current (CVM operation mode) vs. incident radiation power, and fourth column the output current for constant voltage mode (CVM).  $T^+$  and  $P_{\max}$  mark the end of the linear response range. The bias 40mV (solid line in panels d, h and l) optimizes  $P_{\max}$  in CVM operation.

The results of our simulations for the *UD-1 zone* case are shown in the first row of Fig. 1. In particular, Fig. 1(b) displays the computed sheet resistance  $R_{\text{sq}}(T)$  curve. We mark with arrows in that figure the bath temperature 4.2 K and the highest temperature  $T^+$  up to which  $R_{\text{sq}}(T)$  is linear in the transition, used to calculate TCR in Eq. 13. In Fig. 1(c) we show the output voltage of the TES sensor as a function of incident optical power  $P$ , assuming CCM operation with a typical value of the bias intensity,  $I_{\text{bias}} = 10\mu\text{A}$ . We indicate in that figure the  $P_{\text{max}}$  obtained from that curve. In Fig. 1(d) we assume CVM operation and show the corresponding output intensity as a function of  $P$ . When plotting the CVM outputs in this paper we will always display the results for two different bias  $V_{\text{bias}}$ : One that maximizes the obtained  $P_{\text{max}}$  and a second one that illustrates that using different  $V_{\text{bias}}$  would change the shape of the output curve and thus degrade (to a different degree depending on the considered film) the range of incident power for which linear and non-saturated response is observed (a feature that is not observed for the CCM mode).<sup>3</sup>

The numerical values resulting from those simulations for the main bolometric performance parameters are summarized in Table 1, including TCR,  $P_{\text{min}}$ ,  $P_{\text{max}}$  and dynamic range DR for both CCM and CVM operations. As may be seen in those results, the non-patterned film with underdoped carrier density  $\bar{p} = 0.060$  is valid as a bolometer with operating temperature 4.2 K, but with a modest performance (ultimately associated with its low value of  $T^+$ , of about just 1 K above 4.2 K).

Our similar results for the non-patterned film with overdoped carrier density  $\bar{p} = 0.260$ , labeled *OD-1 zone*, are shown in the first row of Fig. 2 and Table 1. Again the low  $T^+$  induces a quite modest bolometric performance, much worse than the ones we shall obtain for planar-patterned  $\bar{p}(\vec{r})$  films.

An interesting difference between the underdoped and overdoped cases is that  $P_{\text{max}}$  is achieved at quite different  $V_{\text{bias}}$  when in CVM mode (see Figs. 1(d) and 2(d)). The reason may be traced back to their normal-state background contributions to the electrical resistivity (different to each other in magnitude and  $T$ -behavior, compare

---

<sup>3</sup>The reason why a variation of  $V_{\text{bias}}$  affects  $P_{\text{max}}$  is: For a bias that is too low the output  $I$  grows in CVM mainly as  $R^{-1}$  and hence is not linear in  $P$ , while for a bias that is too large the range of significant response to incident power is reduced because  $TP=0$  is already well above 4.2 K due to self-heating in Eqs. 10 to 12. Thus, the optimum  $P_{\text{max}}$  is achieved for an intermediate value of  $V_{\text{bias}}$ . (For CCM instead, our  $I_{\text{bias}}$  values produce small self-heating and the output grows with  $R$ ).

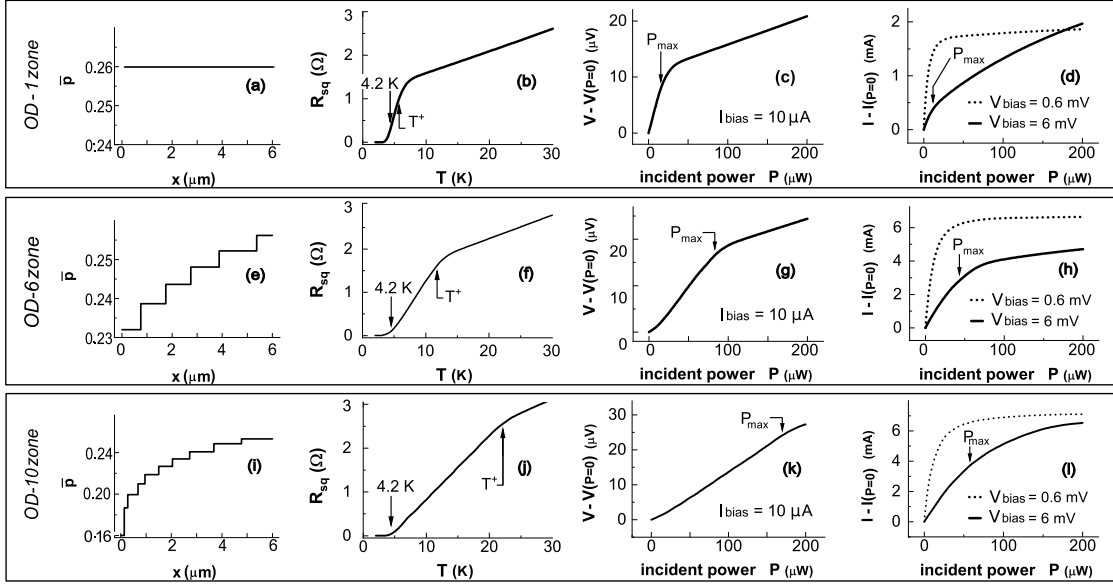


Figure 2: Results for films with nominal carrier densities in the underdoped (OD) range,  $\bar{p} > 0.16$ . Symbol meanings and panel organization are the same as in Fig. 1. The bias 6mV (solid line in panels d, h and l) optimizes  $P_{\max}$  in CVM operation.

Figs. 1(b) and 2(b)).

Finally for the non-patterned films, let us note here that they give us the chance to test the validity of our  $R(T)$  simulation procedures against experimental results. This is because measurements of  $R(T)$  do exist in the literature for non-patterned LSCO films with  $T_c$  near the value 4.2K. In Fig. 3 we compare the experimental data measured by Shi and coauthors (taken from [45]) and our simulation results done with the methods described before and assuming a  $\bar{p}$  value within about 10% of the one estimated in [45] for that sample. The agreement is excellent. Unfortunately, no direct measurements of  $P_{\max}$  and  $P_{\min}$  seem to exist in a film of that composition, to our knowledge never yet experimentally implemented as sensor element in a TES device. For other  $\bar{p}$  values (but then  $T_c$  quite different from 4.2K) the interested reader may find in Ref. [42] further comparisons between experimental  $R(T)$  data in non-patterned films and computer simulations using a methodology not too different from the one in the present work, further confirming the basic validity of our present simulation procedures.

## 4 Results for patterned underdoped superconductors (*UD-N zone*)

We move now to the case in which a  $\bar{p}(\vec{r})$  spatial pattern is imposed, considering in this Section the underdoped range  $\bar{p} < 0.16$ .

As discussed in Sect. 2, we run simulations that scan numerous different patterns, and select the ones with better bolometric performance. In doing so, we found that a pattern consisting of a relatively modest number  $N = 6$  of spatial zones of different nominal carrier concentrations is already able to provide significantly better results than non-patterned films. We label that six-zone structure as *UD-6 zone*. The main parameter values in Eqs. 8 and 9 defining the patterning are listed in Table 1. Also, the  $\bar{p}(x)$  profile is plotted in Fig. 1(e) (and it is the example pictured in our graphical abstract)

The bolometric behavior for such structured film is shown in the second row of Fig. 1. In particular, Fig. 1(f) displays the computed  $R_{\text{sq}}(T)$  curve, Fig. 1(g) the resulting output versus incident power for CCM operation and Fig. 1(h) the corresponding output versus incident power for CVM. The resulting performance parameters are summarized in Table 1.

It is easy to see that the obtained sensing characteristics display a very significant improvement when compared with the non-patterned *UD-1 zone*: Notably, the dynamic range improves by about one order of magnitude in both CCM and CVM operation, mainly driven by the significant increase of  $P_{\text{max}}$  in both modes ( $P_{\text{min}}$ , on the other hand, experiences more moderate changes). The temperature range of operation is also significantly widened ( $T^+$  becomes now about 8 K above liquid-He temperature). Note also that the increase in DR does not come at the expense of weaker TCR: On the contrary, Table 1 shows that TCR is in fact also improved (by more than 50%).

We also report (see Fig. 1(i) to (l) and Table 1) on the results obtained for a probably more difficult-to-fabricate pattern with  $N = 10$  zones (labeled as *UD-10 zone*) that provides even better results. This pattern further extends the linear operation range to be about  $T^+ - 4.2 \text{ K} \simeq 14 \text{ K}$  and also further improves  $P_{\text{max}}$ , without dramatically



affecting  $P_{\min}$  or TCR. The dynamic range DR is correspondingly enlarged over the one of the simpler 6-zone structuration. That being said, the improvements of *UD-10 zone* vs. *UD-6 zone* are well smaller than the ones of *UD-6 zone* vs. *UD-1 zone*.

Very noticeable is the fact that the above quantities for DR are very competitive even when compared with the best values being reported in the literature for TES bolometers for 4.2 K operation using low- $T_c$  superconductors (see, *e.g.*, [65]). Note also that we obtain those good performances already in CCM operation. In fact, they are better for CCM than for CVM. As already commented, CVM is usually more difficult to effectively implement. Our results suggest that operating a planar-patterned cuprate superconducting thin film in its ohmic linear-in- $T$  region with a simple reading based on good quality but conventional volt-meters of about  $10^{-4}$  relative resolution may provide an alternative path for TES bolometer designs at liquid-He base operation temperature.

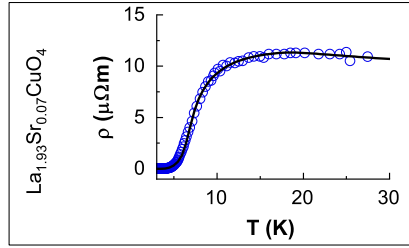


Figure 3: Comparison of the electrical resistivity (circles) measured by X. Shi and coauthors (taken from [45]) in a LSCO films with  $T_c$  of about 4.2 K, with our model equations (solid line). The Sr content estimated in [45] for this sample was about 0.07 and we employed carrier densities within about 10% of that value so to better match  $T_c$  (as the exact value of the latter depends also on the precise film thickness and chemistry of the substrate supporting the film, see Sect. 6).

## 5 Results for patterned overdoped superconductors (*OD-N zone*)

We consider now films with nominal carrier concentration patterns consisting on various zones in the overdoped (OD) range.

Similarly as in the previous Section, we ran simulations scanning numerous differ-

ent patterns and selected the ones with best bolometric performance. We detail in Table 1 the geometry parameters defining them via Eqs. 8 and 9. Their  $\bar{p}(x)$  profiles are displayed in the first column of Fig. 2.

The first pattern, that we label *OD-6 zone*, is composed by six zones that produce the same operating temperature range  $T^+ - 4.2$  K than its underdoped counterpart (about 8 K). The Fig. 2(f) displays the computed  $R_{\text{sq}}(T)$  curve, Fig. 2(g) the resulting output versus incident power for CCM operation and Fig. 2(h) the output versus incident power for the CVM case. As in the underdoped case, already this relatively simple 6-zone option significantly improves the bolometric performance with respect to the non-patterned film (*OD-1 zone*), mainly for  $P_{\text{min}}$ ,  $P_{\text{max}}$  and DR (the latter improving by about one order of magnitude). The patterning even improves the TCR sensibility.

To complete our study, we also considered 10-zone patterns. Our computations resulted in the structure *OD-10 zone* (see Table 1 and third row of Fig. 2). It may be seen that with respect to *OD-6 zone* this 10-zone pattern again improves  $P_{\text{max}}$  and DR, though at the expense of a slight increase of  $P_{\text{min}}$ . This structuration has the largest  $T^+$  of all the reported in this paper,  $T^+ - 4.2$  K = 22 K. We conclude that, also in the overdoped case, 10-zone patterns have the potential of moderate improvements over the 6-zone option, to be pondered against the probable increase in manufacturing difficulty.

Similarly as for the underdoped case, our patterns allow operation in a simple CCM mode and in an ohmic region of the material, with no obvious advantage when using the more elaborate CVM. The reason for this may be traced back to the operating range being wide in temperature, what makes less critical the self-heating effects when compared to TES sensors with much narrow transitions. Naturally this wide operating range is also key for the large obtained DR, competitive with some of the best until now reported for TES bolometers [65] without apparent need for SQUID readout stages.

Some important differences with respect to the underdoped case are also observed: For instance, the  $R_{\text{sq}}$  values in the upper part of the transition are smaller by about one order of magnitude, and also have different  $T$ -dependence after the linear transition region. (This in fact is one of the main reasons for the values of patterning parameters  $\gamma$  and  $\beta$  being quite different to the underdoped case; the other being the  $\bar{p}=1/8$

depression of  $T_c$ ). The variation in  $R_{sq}$  values are also responsible for the quite different optimal bias voltages for the CVM modes in the underdoped and overdoped cases, a fact that may be of relevance in applications. Also, the  $P_{min}$  of the underdoped structurations significantly differ from those of their overdoped counterparts, especially for CVM operation.

## 6 Conclusions and additional considerations for future work

In summary, we have presented methods to calculate the effects of carrier density structuration and patterning over the resistive transition  $R(T)$  of thin films of the high-temperature superconductor  $\text{La}_{2-x}\text{Sr}_x\text{CuO}_{4+y}$  (LSCO) and their corresponding characteristics as sensing surface for resistive transition-edge bolometer detectors (TES) operating at a base temperature 4.2 K convenient for liquid-He cryogenics. We also deploy ad-hoc computer search algorithms to discover the carrier density maps that optimize such sensing performance. We consider two major contributions to structuration: The Gaussian-random nanoscale disorder associated to carrier density nonstoichiometry, plus the imposition of regular arrangements of zones with different nominal carrier densities (patterning).

When applied to non-patterned films, our model is in good agreement with existing measurements of  $R(T)$ .

When considering patterns composed of various zones of nominal carrier densities, our methods identify designs with either underdoped or overdoped carrier densities that markedly improve the saturation power and dynamic range of the TES detector and present favorable sensitivity even in the easy-to-implement constant current mode of measurement.

Our results indicate that structured LSCO thin films are promising candidates for TES operating at liquid-He temperature and, therefore, we suggest experimental workers to pursue their fabrication using our pattern designs as guidelines. As such, we believe that various considerations for those further works may be pertinent here:

*i)* Firstly, note that, as already mentioned in this article, for a good account of the resistive transition it is crucial to take random disorder into account. We showed that our procedures (here including in particular our Eq. 7 for estimating the intrinsic, unavoidable disorder due to nonstoichiometry for each nominal  $\bar{p}$ ) are accurate for good quality films with disorder in the intrinsic limit (see Sect. 3 or Fig. 3). However, it is conceivable that maybe some pattern fabrication methods could, as a side-effect, induce additional disorder contributions. Thus, it seems prudent that experimentalists check for possible nonuniversal additional contributions to Eq. 7 in their films (for what we suggest to measure the resistive transition after inducing just a uniform 1-zone pattern). *ii)* Secondly, experimental details such as sample thickness may also induce small changes for both  $T_c(p)$  and  $\rho_n(T, p)$  with respect to our Eqs. 1 to 3. We do not find however strong changes in our results when considering moderate changes for the parameters in those equations (those expected for moderate deviations from thickness 100 nm) unless that the  $\bar{p}(\vec{r})$  values must be shifted to match the operational temperature 4.2 K (in other words, for those small changes the newly obtained  $\bar{p}(\vec{r})$  patterns basically shift to reproduce the former  $T_c(\vec{r})$  pattern).

In any case, the authors hereby express their willingness to help, if contacted, in repeating the type of simulations detailed in this article with parameters or phenomenological relationships custom-tuned to the possible specificities of those eventual experimental efforts.

**Acknowledgements.**— We acknowledge support by University of Santiago de Compostela, Project 2024-PU036 ‘Propiedades de materiales superconductores micro e nanoestructurados’. MMB was supported by Ministerio de Universidades, Spain, through National Program FPU (grant number FPU19/05266).

## References

- [1] Z. Vafapour, M. Dutta, and M.A. Stroschio, “Sensing, Switching and Modulating Applications of a Superconducting THz Metamaterial,” *IEEE Sensors Journal*, vol. 21, pp. 15187-15195, 2021, doi: 10.1109/JSEN.2021.3073078.

- [2] L. Yang *et al.*, “The In-Plane Magnetic Field Measurement Method of SC/MR Mixed Sensor and Its Three-Axis Magnetic Sensor With Integrated Magnetic Concentrator,” *IEEE Sensors Journal*, vol. 23, pp. 240-246, 2023, doi: 10.1109/JSEN.2022.3221721.
- [3] M. H. Amini, A. Ghorbani, and A. Abdipour, “Field Analysis for Superconducting Grounded Coplanar Waveguide Transmission Lines,” *IEEE Sensors Journal*, vol. 24, pp. 8064-8070, 2024, doi: 10.1109/JSEN.2024.3358009.
- [4] M.B. Brock, E.V. Østergaard, M. Busi *et al.*, “Superconducting transition edge bolometer for high-flux neutron detection,” *Sci. Rep.*, vol. 13, pp. 22266-1–16, 2023, doi: 10.1038/s41598-023-49469-4.
- [5] A. Badía-Majós *et al.*, “Laser nanostructured metasurfaces in Nb superconducting thin films,” *Appl. Surf. Sci.*, vol. 649, pp. 159164-1–12, 2024, doi: 10.1016/j.apsusc.2023.159164.
- [6] A.E. Lita, A.J. Miller, and S.W. Nam, “Counting near-infrared single-photons with 95% efficiency,” *Optics Express*, vol. 16, pp. 3032-3040, 2008, doi: 10.1364/OE.16.003032.
- [7] J.N. Ullom, and D.A. Bennett, “Review of superconducting transition-edge sensors for x-ray and gamma-ray spectroscopy,” *Supercond. Sci. Technol.*, vol. 28, pp. 084003-1–36, 2015, doi: 10.1088/0953-2048/28/8/084003.
- [8] P.L. Richards, “Bolometers for infrared and millimeter waves,” *J. Appl. Phys.*, vol. 76, pp. 1-24, 1994, doi: 10.1063/1.357128.
- [9] M. Dobbs *et al.*, “Frequency multiplexed superconducting quantum interference device readout of large bolometer arrays for cosmic microwave background measurements,” *Rev. Sci. Instr.*, vol. 83, pp. 073113-1–25, 2012, doi: 10.1063/1.4737629.
- [10] R.W. Romani, A.J. Miller, B. Cabrera, S.W. Nam, and J.M. Martinis, “Phase-resolved Crab studies with a cryogenic transition-edge sensor spectrophotometer,” *ApJ*, vol. 563, pp. 221–228, 2001, doi: 10.1086/323874.

- [11] P.C. Nagler, J.E. Sadleir, and E.J. Wollack, “Transition-edge sensor detectors for the Origins space telescope,” *J. Astron. Telesc. Instrum. Syst.*, vol. 71, pp. 011005-1–18, 2021, doi: 10.1117/1.JATIS.7.1.011005.
- [12] D.A. Harper *et al.*, “HAWC+, the far-infrared camera and polarimeter for SOFIA,” *J. Astron. Instrum.*, vol. 7, pp. 1840008-1–41, 2018, doi: 10.1142/S2251171718400081.
- [13] G.C. Jaehning *et al.*, “Development of space optimized TES bolometer arrays for LiteBIRD,” *J. Low Temp. Phys.*, vol. 199, pp. 646-653, 2020, doi: 10.1007/s10909-020-02425-2.
- [14] M.B. Brock, E.V. Østergaard, M. Busi, A.C. Wulff, A.B. Abrahamsen, and L.T. Kuhn, “Superconducting transition edge bolometer for high-flux neutron detection,” *Scientific Reports*, vol. 13, pp. 22266-1–15, 2023, doi: 10.1038/s41598-023-49469-4.
- [15] M. Varnava, D.E. Browne, and T. Rudolph, “How good must single photon sources and detectors be for efficient linear optical quantum computation?,” *Phys. Rev. Lett.*, vol. 100, pp. 060502-1–4, 2008, doi: 10.1103/PhysRevLett.100.060502.
- [16] I. Charaev *et al.*, “Single-photon detection using high-temperature superconductors,” *Nat. Nanotechnol.*, vol. 18, pp. 343-349, 2023, doi: 10.1038/s41565-023-01325-2.
- [17] J. Chang, and I.E. Zadeh, “Superconducting single-photon detectors get hot,” *Nat. Nanotechnol.*, vol. 18, pp. 322-323, 2023, doi: 10.1038/s41565-023-01334-1.
- [18] K.D. Irwin, “An application of electrothermal feedback for high resolution cryogenic particle detection,” *Appl. Phys. Lett.*, vol. 66, pp. 1998-2000, 1995, doi: 10.1063/1.113674.
- [19] R. Mohajeri, Y.A. Opata, A.C. Wulff, J.C. Grivel, and M. Fardmanesh, “All metal organic deposited high- $T_c$  superconducting transition edge bolometer on yttria-stabilized zirconia substrate,” *J. Supercond. Nov. Magn.*, vol. 30, pp. 1981-1986, 2017, doi: 10.1007/s10948-016-3805-7.

- [20] M.J.M.E. de Nivelles *et al.*, “Low noise high- $T_c$  superconducting bolometers on silicon nitride membranes for far-infrared detection,” *J. Appl. Phys.*, vol. 82, pp. 4719-4726, 1997, doi: 10.1063/1.366327.
- [21] P. Probst *et al.*, “ $\text{YBa}_2\text{Cu}_3\text{O}_{7-\delta}$  quasioptical detectors for fast time-domain analysis of terahertz synchrotron radiation,” *Appl. Phys. Lett.*, vol. 98, pp. 043504-1-4, 2011, doi: 10.1063/1.3546173.
- [22] H. Neff *et al.*, “Nonlinearity and electrothermal feedback of high  $T_c$  transition edge bolometers,” *Appl. Phys. Lett.*, vol. 76, pp. 640-642, 2000, doi: 10.1063/1.125844.
- [23] H. Neff *et al.*, “Noise, bolometric performance and aging of thin high  $T_c$  superconducting films on silicon membranes,” *Thin Solid Films*, vol. 324, pp. 230-238, 1998, doi: 10.1016/S0040-6090(98)00369-1.
- [24] J.C. Verde, A.S. Viz, M.M. Botana, C. Montero-Orille, and M.V. Ramallo, “Calculations of some doping nanostructurations and patterns improving the functionality of high-temperature superconductors for bolometer device applications,” *Nanomaterials*, vol. 10, pp. 97-1-20, 2020, doi: 10.3390/nano10010097.
- [25] Y. Yang, X. Zhang, L. Qin, Q. Zeng, X. Qiu, and R. Huang, “Probing nanoscale oxygen ion motion in memristive systems,” *Nat. Comm.*, vol. 8, pp. 15173-1-10, 2017, doi: 10.1038/ncomms15173.
- [26] I. García-Serrano *et al.*, “Superconducting nanostructures grown by focused ion beam induced deposition”, in *Proceedings of the International Conference on Nano Confined Superconductors and Their Application*, Garmish, Germany, 3-7 September 2016.
- [27] W. Lang, “Nanostructured superconductors,” in: T. Chakraborty (Ed.) *Encyclopedia of condensed matter physics (2nd Ed.)*, Academic Press, Oxford, 2024, pp. 368-380. doi: 10.1016/b978-0-323-90800-9.00014-7
- [28] U.P. Oppenheim, M. Katz, G. Koren, E. Polturak, and M.R. Fishman, “High temperature superconducting bolometer,” *Physica C*, vol. 178, pp. 26-28, 1991, doi: 10.1016/0921-4534(91)90153-P.

- [29] Y. Ando, S. Komiya, K. Segawa, S. One, and Y. Kurita, “Electronic phase diagram of high- $T_c$  cuprate superconductors from a mapping of the in-plane resistivity curvature,” *Phys. Rev. Lett.*, vol. 26, pp. 267001-1–4, 1993, doi: 10.1103/PhysRevLett.93.267001.
- [30] R.A. Cooper *et al.*, “Anomalous criticality in the electrical resistivity of  $\text{La}_{2-x}\text{Sr}_x\text{CuO}_4$ ,” *Science*, vol. 323, pp. 603-606, 2009, doi: 10.1126/science.1165015.
- [31] F. Mahmood, D. Ingram, J.A. Clayhold, I. Božović, and N.P. Armitage, “Effect of radiation-induced defects on the superfluid density and optical conductivity of overdoped  $\text{La}_{2-x}\text{Sr}_x\text{CuO}_4$ ,” *Phys. Rev. B*, vol. 105, pp. 174501-1–8, 2022, doi: 10.1103/PhysRevB.105.174501.
- [32] R. Arpaia, E. Andersson, E. Tralbaldo, T. Bauch, and F. Lombardi, “Probing the phase diagram of cuprates with  $\text{YBa}_2\text{Cu}_3\text{O}_{7-\delta}$  thin films and nanowires,” *Phys. Rev. Mater.*, vol. 2, pp. 024804-1–12, 2018, doi: 10.1103/PhysRevMaterials.2.024804.
- [33] O. Meyer *et al.*, “Transport and structure of ion irradiated HTSC thin films,” *Nucl. Instrum. Methods Phys. Res.*, vol. 65, pp. 539-545, 1992, doi: 10.1016/0168-583X(92)95101-V.
- [34] J. Mosqueira, L. Cabo, and F. Vidal, “Structural and  $T_c$  inhomogeneities inherent to doping in  $\text{La}_{2-x}\text{Sr}_x\text{CuO}_4$  superconductors and their effects on the precursor diamagnetism,” *Phys. Rev. B*, vol. 80, pp. 214527-1–8, 2009, doi: 10.1103/PhysRevB.80.214527.
- [35] W. Lang *et al.*, “Masked ion beam irradiation of high-temperature superconductors: patterning of nano-size regions with high point-defect density,” *Int. J. Nanotechnol.*, vol. 6, pp. 704-714, 2009, doi: 10.1504/IJNT.2009.025308.
- [36] M. Karrer *et al.*, “Vortex matching at 6T in  $\text{YBa}_2\text{Cu}_3\text{O}_{7-\delta}$  thin films by imprinting a 20-nm periodic pinning array with a focused helium-ion beam,” *Phys. Rev. A*, vol. 22, pp. 014043-1–11, 2024, doi: 10.1103/PhysRevApplied.22.014043.



- [37] K. Cho, M. Kończykowski, S. Teknowijoyo, M.A. Tanatar, and R. Prozorov, “Using electron irradiation to probe iron-based superconductors,” *Supercond. Sci. Technol.*, vol. 31, pp. 064002-1–19, 2018, doi: 10.1088/1361-6668/aabfa8.
- [38] S.K. Tolpygo, J.Y. Lin, M. Gurvitch, S.Y. Hou, and J. Phillips, “Effect of oxygen defects on transport properties and  $T_c$  of  $\text{YBa}_2\text{Cu}_3\text{O}_{6+\delta}$ : Displacement energy for plane and chain oxygen and implications for irradiation-induced resistivity and  $T_c$  suppression,” *Phys. Rev. B*, vol. 53, pp. 12462–12474, 1996, doi: 10.1103/PhysRevB.53.12462.
- [39] J.P. Killgore, W. King, K. Kjoller, R.M. Overney, “Machining oxide thin films with an atomic force microscope: Pattern and object formation on the nanometer scale,” *Microscopy Today*, vol. 15, pp. 20-25, 2007, doi: 10.1017/S1551929500051142.
- [40] N. Barišić *et al.*, “Universal sheet resistance and revised phase diagram of the cuprate high-temperature superconductors,” *Proc. Natl. Acad. Sci. U.S.A.*, vol. 110, pp. 12235-12240, 2013, doi: 10.1073/pnas.1301989110.
- [41] Z. Shi, X. Shi, and D. Popović, “Evidence for correlated dynamics near the Berezinskii-Kosterlitz-Thouless-like transition in highly underdoped  $\text{La}_{2-x}\text{Sr}_x\text{CuO}_4$ ,” *Phys. Rev. B*, vol. 94, pp. 134503-1–6, 2016, doi: 10.1103/PhysRevB.94.134503.
- [42] N. Cotón, M.V. Ramallo, and F. Vidal, “Critical temperatures for superconducting phase-coherence and condensation in  $\text{La}_{2-x}\text{Sr}_x\text{CuO}_4$ ”, *arXiv: 1309.5910* [cond-mat.supr-con], pp. 1-16, doi: 10.48550/arXiv.1309.5910.
- [43] T. Timusk and B. Statt, “The pseudogap in high-temperature superconductors: an experimental survey,” *Rep. Prog. Phys.*, vol. 62, pp. 61-122, 1999, doi: 10.1088/0953-8984/20/12/123201.
- [44] N. Cotón, B. Mercey, J. Mosqueira, M.V. Ramallo, and F. Vidal, “Synthesis from separate oxide targets of high quality  $\text{La}_{2-x}\text{Sr}_x\text{CuO}_4$  thin films and dependence with doping of their superconducting transition width,” *Supercond. Sci. Technol.*, vol. 26, pp. 075011-1–11, 2013, doi: 10.1088/0953-2048/26/7/075011.
- [45] X. Shi, Ph.D. dissertation. Florida State University (2012). See also: X. Shi, G. Logvenov, A.T. Bollinger, I. Božović, C. Panagopoulos, and D. Popović, “Emer-

- gence of superconductivity from the dynamically heterogeneous insulating state in  $\text{La}_{2-x}\text{Sr}_x\text{CuO}_4$ ,” *Nat. Mater.*, vol. 12, pp. 47-51, 2013, doi: 10.1038/nmat3487.
- P.G. Baity, X. Shi, Z. Shi, L. Benfatto, and D. Popović, “Effective two-dimensional thickness for the Berezinskii-Kosterlitz-Thouless-like transition in a highly underdoped  $\text{La}_{2-x}\text{Sr}_x\text{CuO}_4$ ,” *Phys. Rev. B*, vol. 93, pp. 024519-1–13, 2016, doi: 10.1103/PhysRevB.93.024519.
- [46] J.W. Loram, K.A. Mirza, J.M. Wade, J.R. Cooper, and W.Y. Liang, “The electronic specific heat of cuprate superconductors,” *Physica C*, vol. 235-240, pp. 134-137, 1994, doi: 10.1016/0921-4534(94)91331-5.
- [47] M.M. Botana and M.V. Ramallo, “A scenario for the critical fluctuations near the transition of few-bilayer films of high-temperature cuprate superconductors,” *Nanomaterials*, vol. 12, pp. 4368-1–17, 2022, doi: 10.3390/nano12244368.
- [48] M. Kofu, S.-H. Lee, M. Fujita, H.-J. Kang, H. Eisaki, and K. Yamada, “Hidden quantum spin-gap state in the static stripe phase of high-temperature  $\text{La}_{2-x}\text{Sr}_x\text{CuO}_4$  superconductors,” *Phys. Rev. Lett.*, vol. 102, pp. 047001-1–4, 2009, doi: 10.1103/PhysRevLett.102.047001.
- [49] K. Yamada *et al.*, “Doping dependence of the spatially modulated dynamical spin correlations and the superconducting-transition temperature in  $\text{La}_{2-x}\text{Sr}_x\text{CuO}_4$ ,” *Phys. Rev. B*, vol. 57, pp. 6165-6172, 1998, doi: 10.1103/PhysRevB.57.6165.
- [50] T.L. Meyer, L. Jiang, S. Park, T. Egami, and H.N. Lee, “Strain-relaxation and critical thickness of epitaxial  $\text{La}_{1.85}\text{Sr}_{0.15}\text{CuO}_4$  films,” *APL Materials*, vol. 3, pp. 126102-1–6, 2015, doi: 10.1063/1.4937170.
- [51] R.I. Rey *et al.*, “The conductivity and the magnetization around  $T_c$  in optimally-doped  $\text{YBa}_2\text{Cu}_3\text{O}_{7-\delta}$  revisited: quantitative analysis in terms of fluctuating superconducting pairs,” *Supercond. Sci. Technol.*, vol. 32, pp. 045009-1–21, 2019, doi: 10.1088/1361-6668/aafe93.
- [52] J. Mosqueira, M.V. Ramallo, S.R. Currás, C. Torrón, and F. Vidal, “Fluctuation-induced diamagnetism above the superconducting transition in  $\text{MgB}_2$ ,” *Phys. Rev. B*, vol. 65, pp. 174522-1–7, 2002, doi: 10.1103/PhysRevB.65.174522.

- [53] C. Carballeira, J. Mosqueira, M.V. Ramallo, J.A. Veira, and F. Vidal, “Fluctuation-induced diamagnetism in bulk isotropic superconductors at high reduced temperatures,” *J. Phys.: Condens. Matter*, vol. 13, pp. 9271-9279, 2001, doi: 10.1088/0953-8984/13/41/316.
- [54] R.A. Klemm, “Phenomenological model of the copper oxide superconductors,” *Phys. Rev. B*, vol. 41, pp. 2073-2097, 1990, doi: 10.1103/PhysRevB.41.2073.
- [55] I. Puica and W. Lang, “Critical fluctuation conductivity in layered superconductors in a strong electric field,” *Phys. Rev. B*, vol. 68, pp. 054517-1–11, 2003, doi: 10.1103/PhysRevB.68.054517.
- [56] C. Carballeira, S.R. Currás, J. Viña, J.A. Veira, M.V. Ramallo, and F. Vidal, “Paraconductivity at high reduced temperatures in  $\text{YBa}_2\text{Cu}_3\text{O}_{7-\delta}$  superconductors,” *Phys. Rev. B*, vol. 63, pp. 144515-1–7, 2001, doi: 10.1103/PhysRevB.63.144515.
- [57] N.E. Hussey, “Phenomenology of the normal state in-plane transport properties of high- $T_c$  cuprates,” *J. Phys.: Condens. Matter*, vol. 20, pp. 123201-1–17, 2008, doi: 10.1088/0953-8984/20/12/123201.
- [58] J.W. Loram, J.R. Cooper, J.M. Wheatley, K.A. Mirza, and R.S. Liu, “Critical and Gaussian fluctuation effects in the specific heat and conductivity of high- $T_c$  superconductors,” *Philos. Mag. B*, vol. 65, pp. 1405–1417, 1992, doi: 10.1080/13642819208215108.
- [59] D. Mihailovic, “Optical experimental evidence for a universal length scale for the dynamic charge inhomogeneity of cuprate superconductors,” *Phys. Rev. Lett.*, vol. 94, pp. 207001-1–4, 2005, doi: 10.1103/PhysRevLett.94.207001.
- [60] M.D. Niemack *et al.*, “A kilopixel array of TES bolometers for ACT: Development, testing, and first light,” *J. Low Temp. Phys.*, vol. 151, pp. 690–696, 2008, doi: 10.1007/s10909-008-9729-2.
- [61] A.J. Miller, S.W. Nam, J.M. Martinis, and A.V. Sergienko, “Demonstration of a low-noise near-infrared photon counter with multiphoton discrimination,” *Appl. Phys. Lett.*, vol. 83, pp. 791-793, 2003, doi: 10.1063/1.1596723.

- [62] A.V. Sergeev *et al.*, “Transparency of a  $\text{YBa}_2\text{Cu}_3\text{O}_{7-\delta}$  film/substrate interface for thermal phonons measured by means of voltage response to radiation,” *Phys. Rev. B*, vol. 49, pp. 9091-9096, 1994, doi: 10.1103/PhysRevB.49.9091.
- [63] J.W. Appel *et al.*, “Calibration of transition-edge sensor (TES) bolometer arrays with application to CLASS,” *ApJS*, vol. 262, pp. 52-1–15, 2022, doi: 10.3847/1538-4365/ac8cf2.
- [64] H. Kraus, “Superconductive bolometers and calorimeters,” *Supercond. Sci. Technol.*, vol. 9, pp. 827-842, 1996, doi: 10.1088/0953-2048/9/10/001.
- [65] D. Fukuda *et al.*, “Absolute power measurement with transition edge sensors and SQUID amplifier,” *J. Phys.: Conf. Ser.*, vol. 43, pp. 1315-1318, 2006, doi: 10.1088/1742-6596/43/1/321.
- [66] J. Clarke, G.I. Hoffer, P.L. Richards, and N.-H. Yeh, “Superconductive bolometers for submillimeter wavelengths,” *J. Appl. Phys.*, vol. 48, pp. 4865-4879, 1977, doi: 10.1063/1.323612.